Thermal-Metallurgical-Mechanical Analysis of Weldment Based on the CFD Simulation

Jason Cheon and Suck-Joo Na

Abstract A new method of numerical thermal-metallurgical-mechanical analysis was introduced in this paper. The CFD welding simulation is based on the mass and heat transfer analysis solving mass, momentum, and energy conservation equations along with the Volume of Fluid (VOF) method. The VOF method is employed to track the shape of the free surface. The arc and droplet heat source model with electromagnetic force and arc pressure model were used for the arc welding process. Next, the temperature history of CFD welding simulation was transferred to the FEM domain for thermal-metallurgical-mechanical analysis with CFD-FEM framework. The diffusion kinetics considered phase transformation model successfully predicted phase fraction and residual stress distribution of carbon steel weldment. By using the combination of suggested T-M-Me analysis method and CFD welding analysis, it is possible to reproduce a phenomenon closer to reality. Also, the recent CFD-based process analyses and results that can be extended to multi-physical analysis were briefly introduced. However, considerable assumptions and simplified models are different from real welding phenomena. To solve this gap and to use welding simulation as a prediction tool rather than a reproduction, many young researchers will need to challenge.

Keywords Computational fluid dynamics · Process model
CFD-FEM framework · Data transfer scheme · Phase transformation
Residual stress

1 Introduction

Numerically predicting a phase transformation and its mechanical effect on carbon steel, begins with a heat treatment process analysis [1]. By considering carbon steel as a solid solution in the diffusion process, the phase fraction will be affected by

J. Cheon · S.-J. Na (✉)
Department of Mechanical Engineering, KAIST, 291 Daehak-ro, Yuseong-gu,
Daejeon 34141, Republic of Korea
e-mail: sjoona@kaist.ac.kr

S. Chen et al. (eds.), *Transactions on Intelligent Welding Manufacturing*,
Transactions on Intelligent Welding Manufacturing,
https://doi.org/10.1007/978-981-10-8330-3_1

chemical composition and temperature history during the cooling process. Consequently, the heat treatment process analysis is based on a time-temperature-transformation (TTT) diagram or continuous cooling transformation (CCT) diagram data for each type of carbon steel. Moreover, for precise estimation of the temperature history, the analysis also focuses on cooling models, including convection and radiation heat loss to the cooling medium. By adding a heating process model, including a heat source, and austenization phase prediction, phase transformation prediction analyses of welding processes have been conducted using the finite element method (FEM) based conductive heat transfer (CHT) analysis [2–6]. According to previous thermal metallurgical welding stress analyses, accounting for the phase transformation effect in the mechanical analysis is important, when considering a welded high carbon steel structure. The residual stress is highly affected by the phase transformation induced strain component, and the phase transformation is highly affected by thermal history.

As a numerical thermal analysis method, FEM-based CHT analysis has been widely used with Gaussian surface flux distribution or double ellipsoidal power density distribution. The double ellipsoidal power density distribution was suggested by Goldak et al. [7] in 1984 as a heat source to reproduce the penetrating action of the arc and droplet, which transports heat well below the surface. Because of their simplicity and accessibility, Gaussian surface flux distribution (or surface heat source, SHS) and double ellipsoidal power density distribution (or volumetric heat source, VHS) are today the most widely employed for analysis of the arc welding process.

However, the FEM-based CHT analysis with VHS has physical limitations in the GMAW process. First of all, artificial thermal properties for the liquid state are required, due to the absence of the advection effect. In the GMAW process, the mass flow of droplets and the arc force driven convective flow on the molten pool diminishes the fusion-zone temperature. The FEM-based CHT analysis achieves a diminished fusion-zone temperature by enhancing the diffusion effect with artificial thermal properties. Nonetheless, the FEM-based CHT analysis with VHS for the GMAW process has been employed until today based on its advantages, which include reasonable calculation speed, the simplicity of the heat source, and good accessibility to the thermo-mechanical analysis.

Meanwhile, computational fluid dynamics (CFD) based mass and heat transfer (MHT) analyses have also been employed for the numerical thermal analysis of welding processes since the early 2000s. The main merit of CFD-based MHT analyses is the ability to consider the advection effect on the molten pool. Because of this advantage, it has been possible to consider the momentum of the molten pool flow, process dependent bead shape, and reasonable molten pool temperature without the use of artificial thermal properties of the liquid state.

Following the development of the image recording technique, the parameters of SHS have been extricated from uncertainty using the measuring arc intensity distribution scheme with high-speed camera image analysis, using the Abel inversion method [8] and Fowler-Milne method [9]. Also, droplet mass and the heat source's parameters (size, velocity, and initial position) were changed from a rough

assumption to measurement based information. However, complex force and pressure models are still required to consider momentum balance with mass balance in the CFD-based MHT analysis. This complexity degrades accessibility and computational calculation speed. Also, the CFD-based MHT analysis result makes it impossible to extend the thermo-mechanical analysis without a special data transfer scheme, even with a reasonable result.

Phase transformation data (TTT and CCT) are built from the constant temperature condition or constant cooling rate condition. The welding process does not occur at a constant temperature and or constant cooling rate, but previous researchers [3–5, 10] have made prediction of phase transformations with additional assumptions and hypothesis. The main target has been the prediction of weldment deformation, but the phase fraction of the weldment has not been validated yet.

The representative numerical stress analysis method used for considering phase transformations during thermal processes is the quenching process stress analysis [11–13]. The phase transformation induced strain values from austenite to bainite or martensite have been experimentally of analytically determined. On the other hand, for the welding process, the phase transformation stress analysis involves both a heating and cooling process. In previous numerical phase transformation considered mechanical analyses, the stress concentration is determined by the induced strain of the phase transformation, and the phase dependent mechanical properties [2–5, 14–16]. Dilatometry data for a constant heating and cooling rate condition has been used to define the dilatometric behavior produced by transformations during the gas tungsten arc (GTA) spot welding process [4], and the hard-face-welding process [14]. Cho and Kim [2] suggested that volumetric strain was induced by a phased fraction based transformation. In the heating process, the ferrite to austenite transformation from AC1 to AC3 produces a phase transformation induced volumetric (TRIV) strain, instead of a thermal expansion strain. In the cooling process, the austenite to martensite transformation was considered with TRIV strain. Also, the phase fraction of martensite was estimated using the welding time constant, Δt_{8-5}. Deng and Murakawa [10] compared the effects of TRIV and phase transformation dependent yield strength on the welding residual strain for the GMAW process. They evolved a transformation model with considering the austenite to bainite transformation [15]. Finally, the transformation induced plastic (TRIP) strain effect [17, 18] was reproduced in the recent literature [5, 16].

In their previous research on in welding procedures, a phase transformation based mechanical analysis was applied to real welding phenomena. However, their model has the potential for further development. If a more reliable metallurgical prediction model can be applied to the mechanical model, the results of a thermal metallurgical mechanical analysis of the weldment would contribute to a better understanding of its natural behavior. Also, a more realistic thermal analysis might lead to more realistic results for the whole procedure.

For extension from the CFD-based MHT analysis result to metallurgical and mechanical analysis of weldment, CFD-FEM framework was presented [19]. By transferring the temperature history from CFD to the FEM domain, the thermal history of a CFD-based MHT analysis can now be used for multi-physics analysis.

This paper presents a brief summary of recent numerical approaches for thermal-metallurgical-mechanical (T-M-Me) analysis of GMAW weldment based on the CFD-FEM framework [19–21]. Also, the CFD based analysis results of various fields that can be extended to multi-physics analysis are introduced.

2 Experiment and Measurement

Table 1 gives the welding conditions used to produce a bead on plate (BOP) welding of 160 × 89 × 6 mm^3 (thickness) AH36 steel plate using the GMAW process. Figure 1a is the schematic of the welding process. Figure 1b

Table 1 Experiment conditions

Feed rate m/min	Current (A)	Voltage (V)	CTWD (mm)	Welding speed (mm/s)	Electrode diameter (mm)	Shielding gas 80% Ar-20%CO_2 (L/min)
7.5	237.7	26.9	28	10	1.2	20

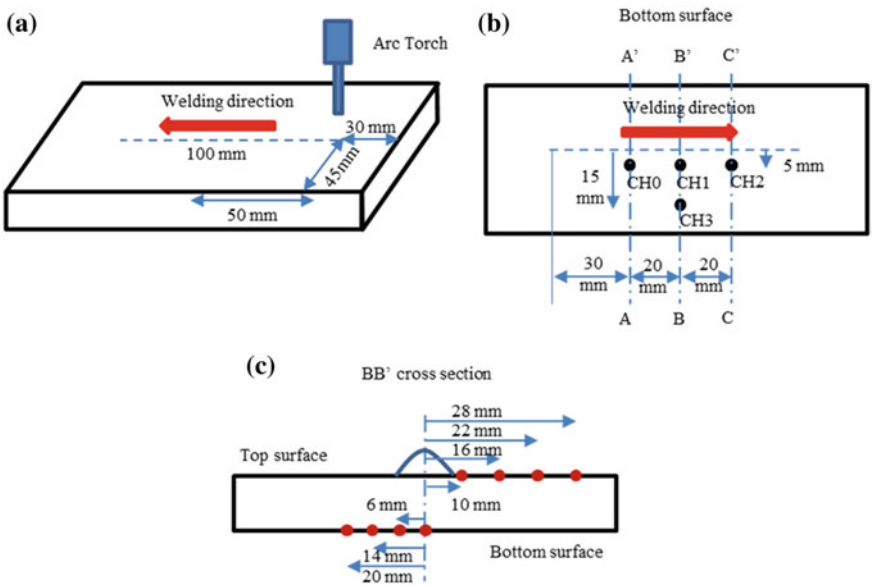

Fig. 1 **a** Schematic of experiment setup; **b** cutting plane and thermocouple position; and **c** positions used to measure directional stress on the BB′ cross section

explains the thermal cycles and the locations used for measuring micro hardness. The instantaneous welding current and voltage data were measured. The welding arc images and droplet transfer were captured using a high-speed camera. The effective radii of arc were extracted from the arc plasma images using the Abel inversion method [35] and the Fowler-Milne method [36]. The droplet information was also extracted by image pixel counting. The weldment cross-sections were cut along the AA′, BB′, and CC′ lines. Next, the cross-section was etched with 2% Nital solution to see the fusion zone (FZ) and the heat affected zone (HAZ). Further, the hardness distribution was measured. Additionally, the BB′ cross-section was etched with Vilella's etchant to distinguish ferrite regions [22]. Figure 1c explains the locations used for measuring directional stress on the top and bottom surfaces.

3 Thermal Analysis

A set of the governing equation were solved with process models for the CFD-based MHT analysis in an incompressible laminar flow condition with Newtonian viscosity model, and calculated in CFD commercial software, Flow3D [23]. The governing equation included the continuity, momentum, energy, and the volume of fluid equation. The energy equation is

$$\frac{\partial h}{\partial t} + \bar{V} \cdot \nabla h = \frac{1}{\rho} \nabla \cdot (k \nabla T) + h_s \tag{1}$$

The advection term (2nd term of left hand side) restrains the increase of the unsteady term (1st term of left hand side) by the diffusivity term and source term (right hand side terms). Once the temperature becomes lower than T_{sol} (or does not exceed it), the advection term returns to zero and it behaves the same as conductive heat transfer. The process models were the arc heat source as a form of double ellipsoidal surface heat source, droplet mass and heat source, arc pressure model, electromagnetic force, drag force, and heat loss model. The detailed procedures and the model descriptions in this chapter have already been explained elsewhere [8, 9, 24]. To ensure agreement of the coordinates and directions of the process model, a fully modeled domain was employed, as shown in Fig. 2.

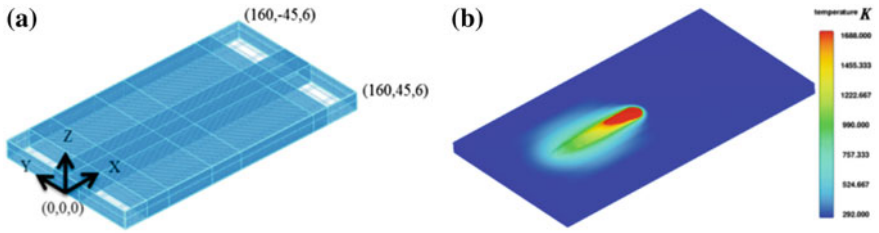

Fig. 2 **a** Solution domain of CFD analysis with coordinate system; **b** temperature distribution at $t = 5$ s

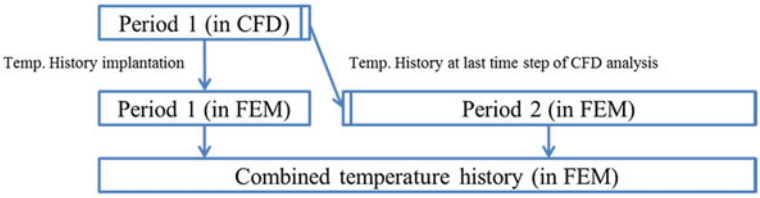

Fig. 3 Schematic description of CFD and FEM combined thermal analysis of GMAW process

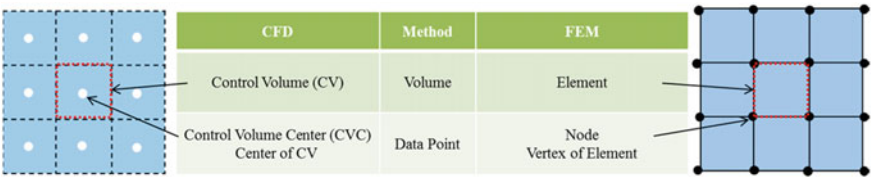

Fig. 4 Schematic descriptions of volume and data points for CFD and FEM configuration

The temperature history was incorporated from the results of two thermal analysis methods for the better accuracy and shortened computational time (Fig. 3). CFD mass and heat flow analysis results were adopted from welding start to solidification (period 1) and FEM conductive thermal analysis results were employed for the cooling process (period 2). As the initial condition for period 2, the temperature distribution of the end step of the period 1 CFD result was applied to the whole solution domain. The same thermal properties were used for continuity of temperature history.

As shown in Fig. 4, the word "node" is a vertex of a polygonised "element" in FEM [25]. The physical and mathematical information were calculated and stored in the node, and the same was also propagated from node to node. On the other hand, the basic unit of configuration in CFD is "control volume" [26]. The calculation and the storing of physical and mathematical data were processed in the Control Volume Center (CVC). For the same size solution domain, the position of the node and CVC are not the same in any density of element or CV. Because of this difference between the two numerical methods, proper data transfer is not possible without a proper data implantation scheme.

To get rid of the mismatched spatial location problem between the node and CVC, a Binary Search Algorithm was employed [27]. In the 3D analysis, the number of CVC's surrounding node is eight. The temperature of a node is calculated by linear interpolation from the eight CVCs (Fig. 5a). In the temperature history of the CFD simulation, spatial temperature distribution data was stored with each discretized time step. Assuming that the temperature fluctuation was not severe within the time step, a linear interpolation scheme was used. Figure 5b represents a schematic of the temporal interpolation.

The Abaqus subroutine was used to achieve temperature history implantation from CFD to FEM in this study. Additionally, a coordinate rotation matrix was used

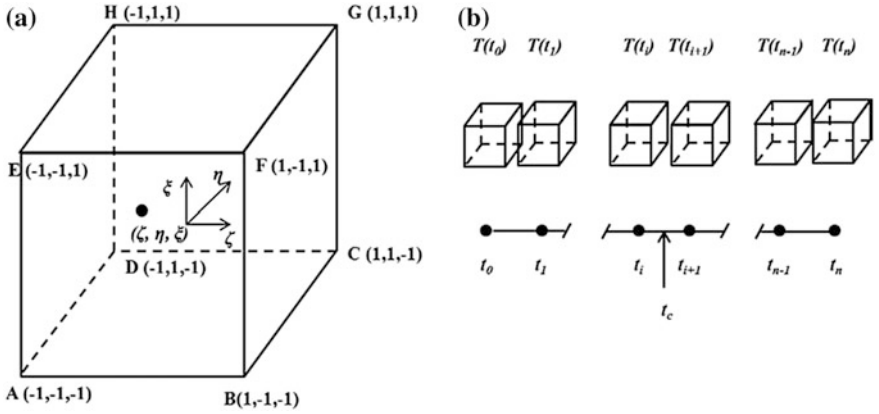

Fig. 5 **a** Schematic diagram of node and surrounding CVCs; **b** schematic diagram of temporal interpolation

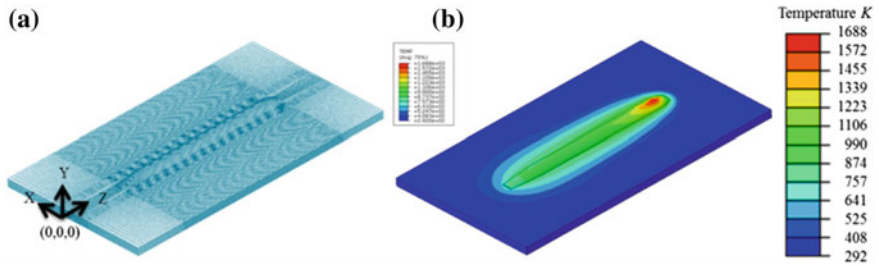

Fig. 6 **a** Solution domain of FEM analysis with coordinate system; **b** temperature distribution at t = 10.9 s (start of period 2)

to take care of the change in domain axis between CFD and FEM (Figs. 2a and 6a). The CFD temperature history was implanted into the FEM solution domain for period 1, and the last time step temperature distribution was set as an initial condition for the FEM conduction heat transfer analysis of period 2, the cooling process.

Figures 7a–c depict the weld pool profiles of the simulation results. The corresponding measured weld micrographs at sections AA′, BB′ and CC′ (as marked in Fig. 1b) are also shown. The red colored area represents the fusion zone of the weldment (peak temperature $\geq$ Ts). Figure 7d presents the variation between the experimental and the calculated weld bead dimensions at the above mentioned three sections. It can be observed that the fusion zone of the weldment has a fingertip shape with slight under-cuts at the end of each bead. As the welding progressed, the penetration depth was increased while the reinforcement height was decreased. The calculated fusion zone profile and its dimensions were in fair agreement with the corresponding experimental results. Figure 7e shows fair good agreement of analysis on temperature history at the four positions marked on the bottom surface of the base plate (Fig. 1b).

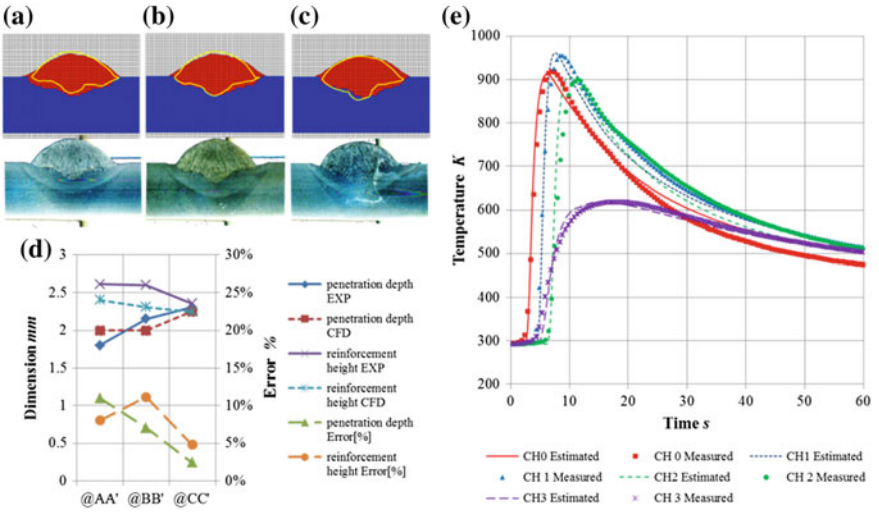

Fig. 7 Simulation and experimental results for the cross-section of **a** AA′; **b** BB′; **c** CC′ (the red colored area is the simulated fusion zone, and solid yellow lines are the boundary of the fusion zone of the experiment); **d** quantified result comparison, and **e** calculated and the corresponding measured temperature history of CH0–CH3

4 Thermal-Metallurgical Analysis

The phase transformation estimation algorithm [19] is based on the fraction conservation relation as below

$$F_{total} = F_f + F_a + F_b + F_m + F_l \tag{2}$$

F_{total} and F_i represent the total fraction sum and the fraction of the i phase. The subscripts f, a, b, m, and l refer to the ferrite, austenite, bainite, martensite and liquid phases. As an initial condition, 100% ferrite fraction was assumed. The existence of the retained austenite and acicular ferrite were ignored to avoid the complexites in the kinematic behavior, as shown in the CCT diagram of AH36 steel [6] (Fig. 8a).

The austenite fraction in the heating process was estimated using linear interpolation between *AC1* and *AC3*. *AC1* and *AC3* were calculated as the fitted power functions of the instant maximum heating rate (HR) with experimental data [28, 29]. The CCT diagram information including the starting temperature, finishing temperature and the maximum phase fraction at a certain cooling rate for each phase transformation were fitted as the price-wised continuous polynomial functions of the instant cooling rate (*CR*). Based on the fitted *CR* dependent transformation information in the cooling process (Fig. 8b), the austenite to ferrite and austenite to bainite fractions were calculated using linear interpolation between transformation starting and finishing temperature. The martensite transformation fraction was calculated by the Koistinen-Marburger (K-M) equation. Also, the hardness

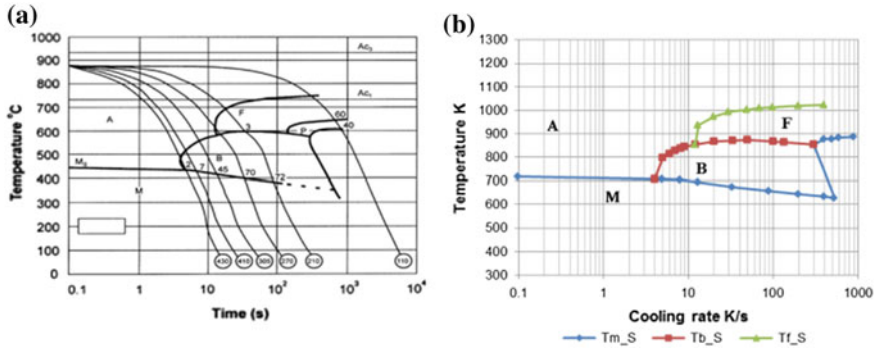

Fig. 8 **a** CCT diagram of AH36 steel and **b** starting temperature versus cooling rate plot for each phase

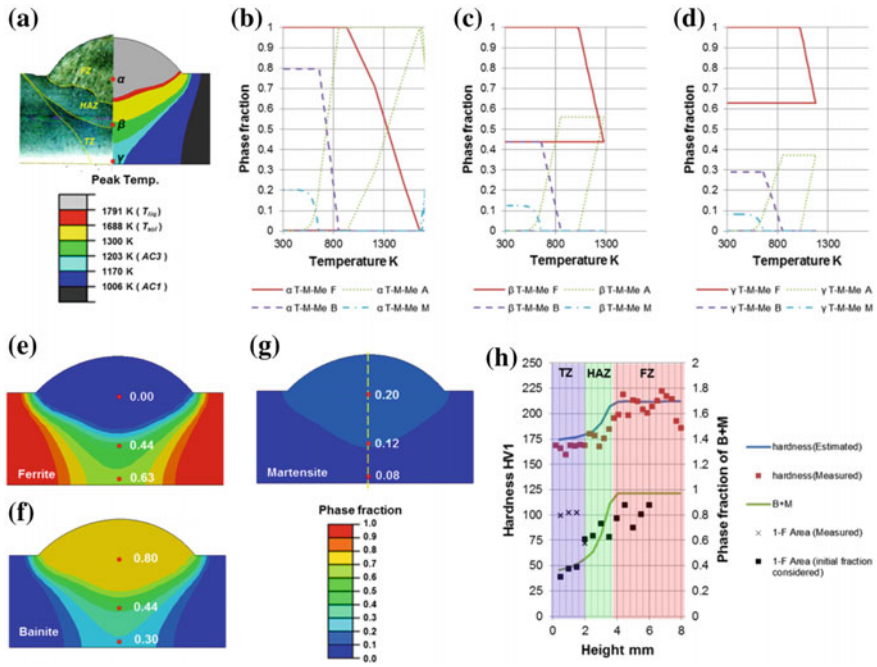

Fig. 9 Phase fraction versus temperature of **b** point α; **c** point β and **d** point γ of **a**, **e**–**g** are the resultant phase fraction distributions on the BB cross section, **h** is a vertical distribution comparison of the estimated versus measured hardness, and the bainite + martensite fraction along the dash-dot line in **g**

estimation was performed using the fitted polynomial function of the martensite fraction based on the CCT diagram hardness information.

The results of the metallurgical analysis is shown in Fig. 9. The phase fraction history of the α, β and γ points (Fig. 9a) are shown in Fig. 9b–d. The final phase

fractions along the BB′ cross-section are shown in Fig. 9e–g. The vertical hardness distribution comparison is explained in Fig. 9h. The hardness of the BB′ cross-section was measured along the dashed yellow line in Fig. 9g. The estimated hardness distribution was higher than the measured distribution due to a high fraction of martensite. However, the steep decline of the HAZ region toward the bottom of the weldment was well estimated. Moreover, a similar trend in hardness was observed in the comparison of the calculated bainite plus martensite fraction distribution and the measured dark area fraction of the etched cross-section of BB′.

5 Thermal-Metallurgical-Mechanical Analysis

The 3-dimensional T-M-Me analysis [21] was conducted using a linear kinematic hardening model with the von Mises yield criteria. The phase fraction information was employed in each subroutine to calculate the elastic, plastic, thermal, TRIV and TRIP strains at every time step. The strain increment balance can be written as below

$$\Delta\varepsilon_{ij} = \Delta\varepsilon_{ij}^{e} + \Delta\varepsilon_{ij}^{p} + \Delta\varepsilon_{ij}^{TH} + \Delta\varepsilon_{ij}^{\Delta V} + \Delta\varepsilon_{ij}^{TRIP} \tag{3}$$

where the superscripts e, p, TH, ΔV and $TRIP$ are the elastic, plastic, thermal, TRIV and TRIP strains. The general behavior of thermal-metallurgical strain (thermal and TRIV strain) with respect to temperature during the welding process can be described using the conceptual schematic in Fig. 10a. In the heating process (red

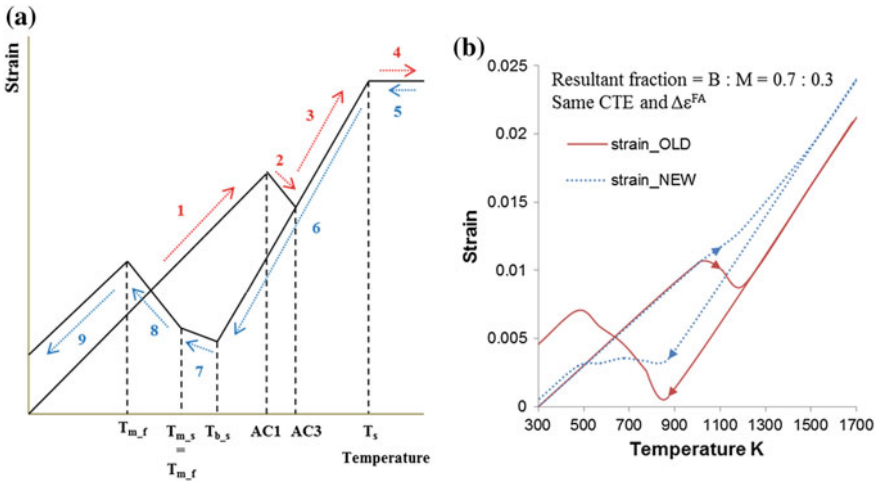

Fig. 10 **a** The schematic of thermal and TRIV strain behavior versus temperature and **b** strain versus temperature curve comparison between previous concept (strain_OLD, solid line) and this study's concept (strain_NEW, dotted line)

arrows), strain increases with increasing temperature, except for the ferrite to austenite transformation (2), while strain decreases with reducing temperature, except for the austenite to bainite transformation (7) and martensite transformation (9) in the cooling process (blue arrows). As noted in previous studies, if the transformation starting and finishing temperatures are fixed and the temperature range is not very wide, TRIV shrinkage (2) and expansion (7, 9) can be determined without considering the thermal expansion of each phase. However, we assumed that the *AC1* and *AC3* were dependent on *HR*, and that temperature range was wide. Therefore, the thermal strain has to be considered in the transformation temperature range. The new concept of overall thermal and TRIV strain behavior can be determined, as below, in relation to increasing temperature ΔT and the coefficient of thermal expansion (CTE) of i phase α_i.

$$\begin{aligned}\Delta\varepsilon^{TH} + \Delta\varepsilon^{\Delta V} = {} & F_F\alpha_F\Delta T + F_A\alpha_A\Delta T + F_B\alpha_B\Delta T + F_M\alpha_M\Delta T \\ & - \Delta\varepsilon^{FA}\Delta F_A + \Delta\varepsilon^{AF}\Delta F_F + \Delta\varepsilon^{AB}\Delta F_B + \Delta\varepsilon^{AM}\Delta F_M\end{aligned} \tag{4}$$

The difference between the old concept from previous studies and the new concept of thermal and TRIV strain behaviors is demonstrated in Fig. 10b.

The resultant response (RES) strain and *YS* distribution on the top surface of the BB′ cross-section are shown in Fig. 11b, c comparing thermal-mechanical (T-Me) analysis results. The differences in the RES strain and *YS* were caused by the phase fraction distribution. Significant differences occurred in the FZ and its neighboring region. Eventually, the von Mises stress was concentrated in the same area on the top (Fig. 11d) and bottom (Fig. 11e) surfaces. A prominent nonlinear resultant

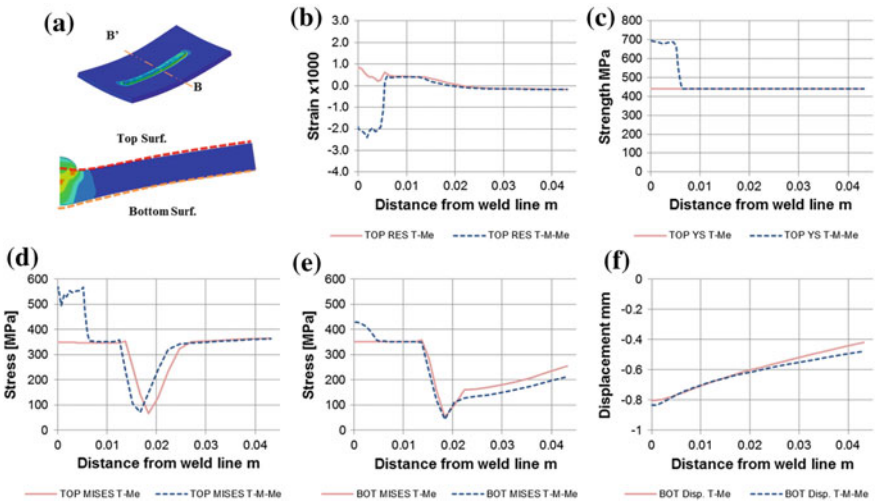

Fig. 11 **a** Is a schematic of the top and bottom surfaces of the BB′ cross-section; **b** and **c** are results for the **b** RES strain and **c** YS distribution on the top surface; **d** and **f** are the results of the von Mises stress distribution on **d** the top surface and **e** bottom surface; **f** is the vertical displacement (u_y) on the bottom surface

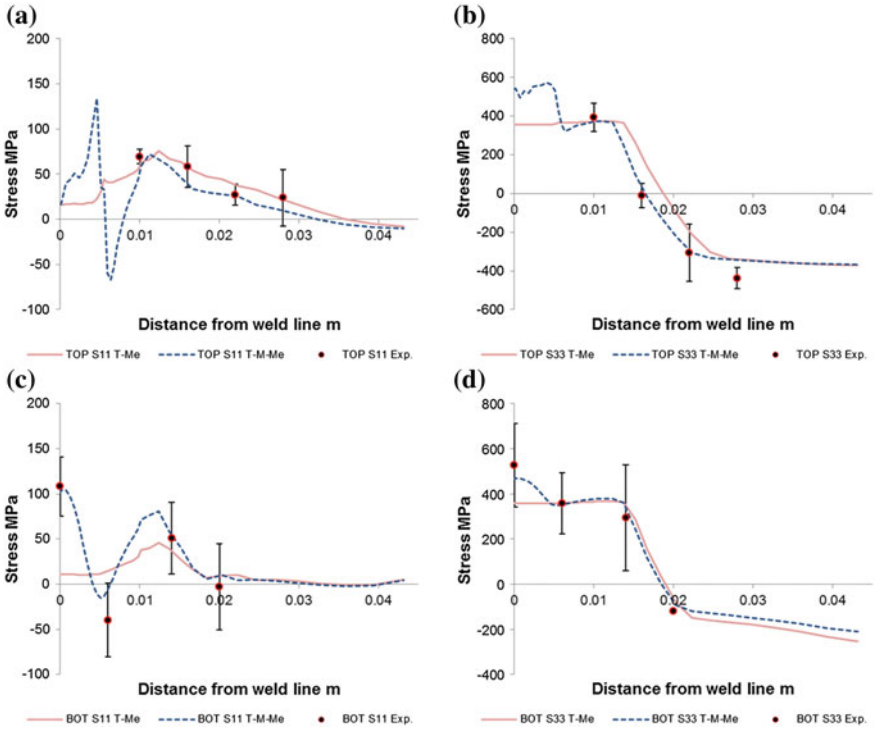

Fig. 12 Comparison of the calculated and measured values of directional stresses on the top surface (**a** transversal and **b** longitudinal) and the bottom surface (**c** transversal and **d** longitudinal)

vertical displacement of the bottom surface (Fig. 11f) was computed in the T-M-Me analysis.

The directional stress distributions on the top and bottom surfaces of the BB′ cross-section are plotted in Fig. 12 along with the values measured (averaged, black dots) at the points in Fig. 1c. The calculated stress distributions of the T-M-Me analysis were well followed measured values than the T-Me analysis. In particular, the nearness of the welding line's fluctuation of stress on the bottom surface confirms the validity of this study's T-M-Me analysis. The comparisons of Fig. 12 confirm the potentials of thermal-metallurgical-mechanical analysis based on the CFD simulation.

6 Extensity of Technique

The CFD-based process analysis can be extended to a multi-physics analysis by the previously described thermal-metallurgical-mechanical analysis technique. Of course, the calculation of the full domain is necessary, and the metallurgical and

mechanical properties of the material must be accompanied. This chapter introduces recent CFD-based process analysis techniques and results that can be extended to multi-physical analysis.

6.1 Arc Welding in Various Conditions

For V-groove welding, the coordinate mapping technique for electromagnetic force model and elliptical symmetric arc model were suggested [30]. Also, asymmetric arc model was adopted for the second pass welding on V-groove weldment [31]. Meanwhile, the process models were formulated in a rotated coordinate system for horizontal fillet joints [32]. The numerical analysis results show high accuracy in various welding speed and wire feed rate conditions (Fig. 13).

Considering heat transfer from arc plasma, droplet and molten slag to material surface, submerged arc welding (SAW) process was simulated [33]. Also two wires [34] and three wire [35] tandem SAW process were well modeled employing arc interaction model. Moreover, the molten pool behavior by flux-wall guided metal transfer was revealed by the predefined solid cavity component [36] (Fig. 14).

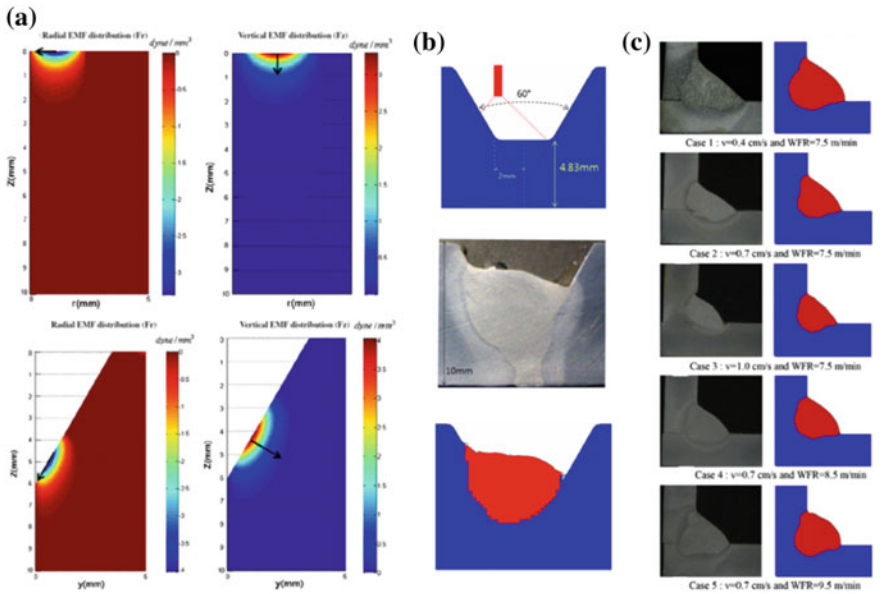

Fig. 13 **a** Comparisons of electromagnetic force of BOP and V-groove feature with mapping technique; **b** schematic and results of experiment and simulation on second pass welding on V-grove; and **c** fusion zone shape comparison of horizontal fillet welding in various process conditions

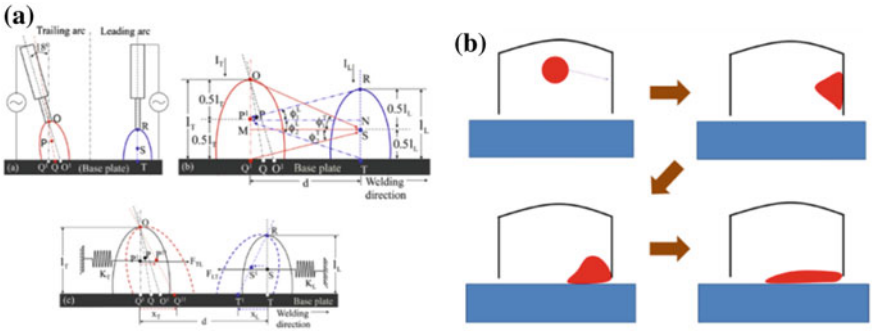

Fig. 14 Schematics of **a** arc interaction model for tandem process and **b** flux-wall guided metal transfer

6.2 *Visualization Using Transient Simulation Result*

Solving unsteady terms of governing equations, the results of CFD based simulation can be utilized for welding phenomena visualization. A numerical research was performed for circumferential welding process on the pipe V-groove in various welding positions by changing gravity direction and root gap [37]. The numerical models not only formed a stable weld bead but also simulated the dynamic molten pool behaviors such as overflow which was not described before. As shown in Fig. 15, without the root gap, it is difficult to form a fully penetrated weld bead in the flat and overhead positions, while humping and melt-through beads are formed in the vertical-upward position under the same welding condition.

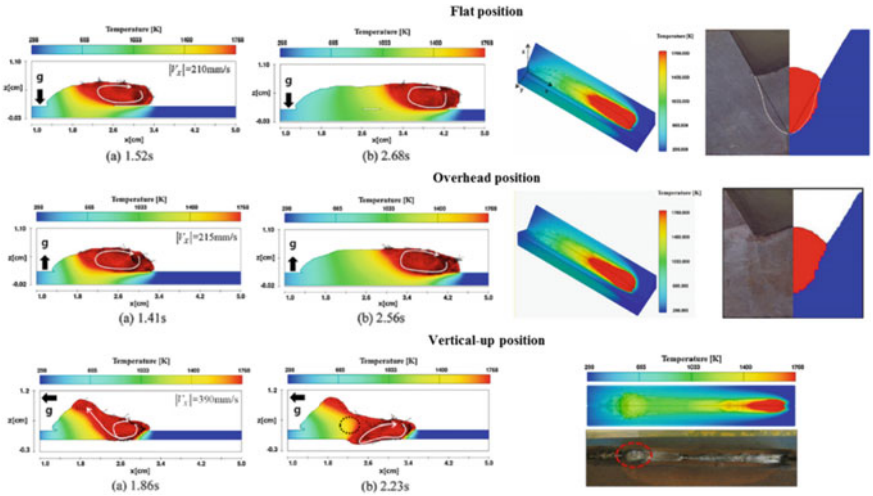

Fig. 15 Flow patterns and comparison simulated bead shape and experiment for non-root gap cases

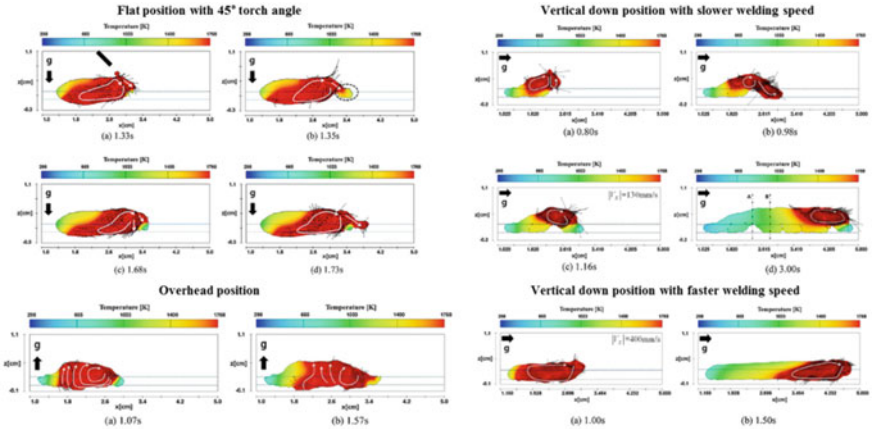

Fig. 16 Flow patterns for 1 mm root gap cases

With a 1-mm root gap as shown in Fig. 16, the molten pool overflow patterns can be described for various welding positions under the given welding conditions. The overflow patterns in some welding positions do not induce the weld defects, while a weld bead with incomplete penetration can be formed in the vertical downward position. Thus, it is necessary to avoid the overflow patterns in such a case by increasing the welding speed.

Meanwhile, a transient welding simulation result was used to visualize momentum flow in the produced fingertip shaped molten pool [38]. In the direct current process, current and voltage are maintained at a constant value. Consequently, only the arc pressure and EMF are used to maintain the molten pool flow. Besides that, the droplet impingement is used to agitate the molten pool flow with a given frequency, even in the DC process. Therefore, investigating the molten pool flow at one droplet intervals could be help to understand the formation of fingertip penetration. Molten pool speed information was utilized to track momentum flow in the weld pool using color maps and streamline plots in various planes (Figs. 17, 18 and 19).

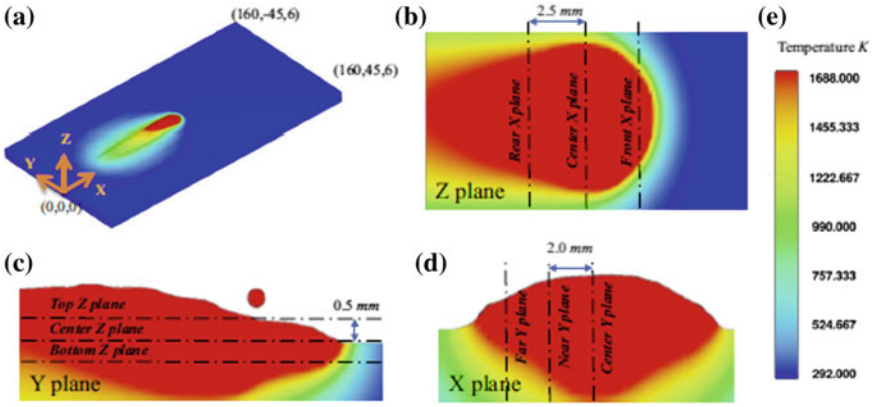

Fig. 17 Analyzed planes in momentum visualization study

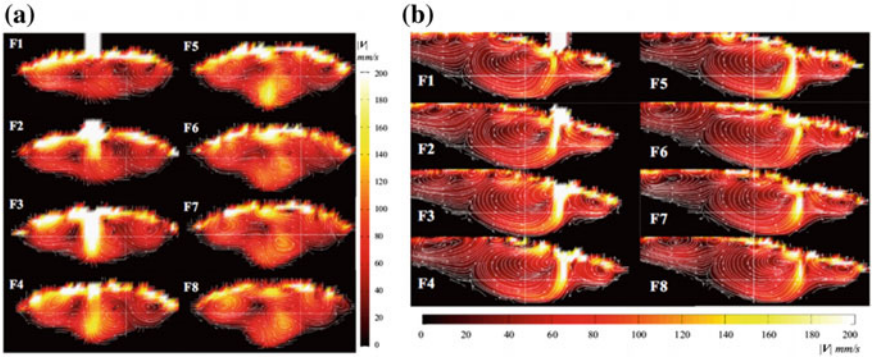

Fig. 18 Momentum flow history of **a** Center X plane and **b** Center Y plane

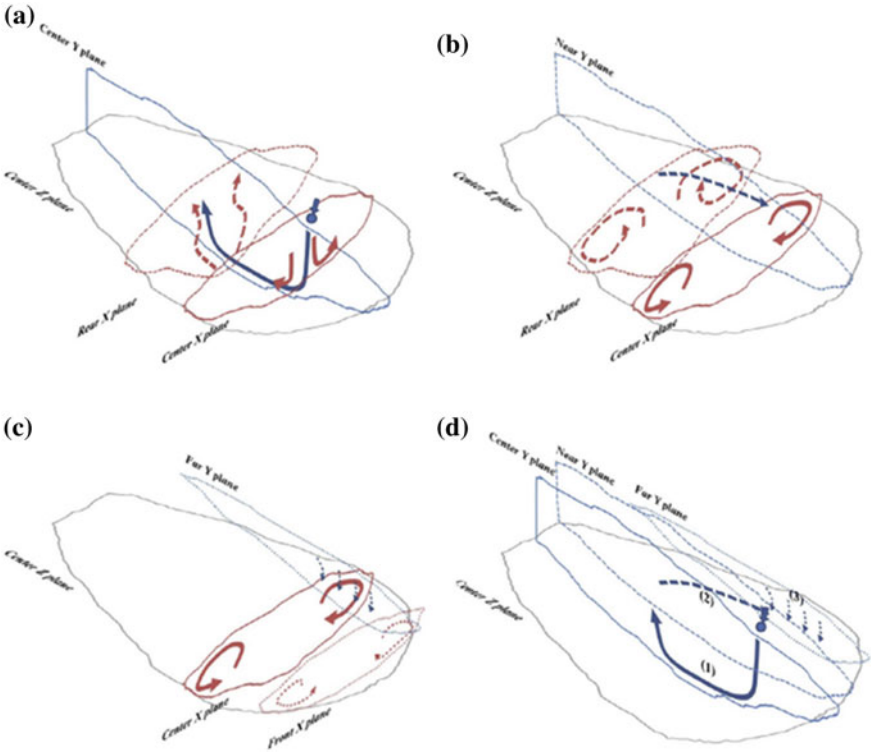

Fig. 19 The schematics of droplet impingement momentum flow on the molten pool, **a** the first effect of the droplet momentum and **b**–**c** secondary effect of droplet momentum (blue arrows are the strongest flow pattern in the *Y*-planes, and red arrows are the most active flow patterns in the *X*-plane); **d** sequential description of droplet impingement momentum flow on *Y*-planes

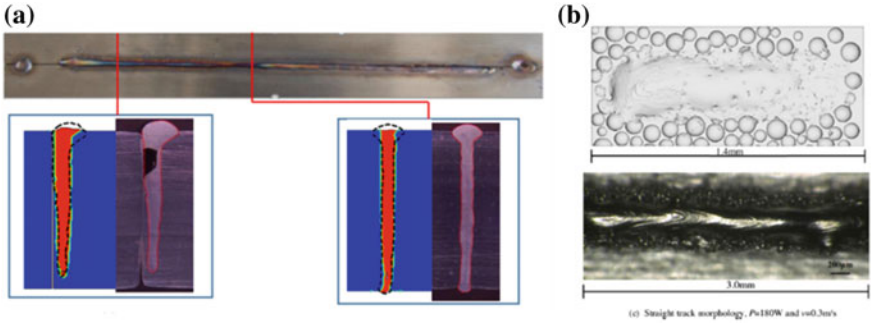

Fig. 20 Comparisons of experiment and simulation for **a** non-zero gap laser butt welding and **b** single layer morphology of selective laser melting process

As results, it was determined that the droplet impingement momentum first strikes the bottom of the molten pool and digs a deep fingertip penetration. Then, the droplet impingement momentum detours backward at a deep level and moves forward at a shallow level, and widens the molten pool width as shown in Fig. 20.

6.3 Laser Processes

The Fresnel's reflection model for multiple reflections of lay with recoil pressure, scattering, and absorption model is utilized for the laser welding process and selective laser melting process. The laser matter interaction techniques were utilized for laser ablation on semi transparent material [39], laser welding process [40–42], and selective laser melting process (SLM) [43].

6.4 Arc-Laser Hybrid Welding Process

The arc and laser welding processes are the most widely used. Great effort is required to understand the physical phenomena of arc and laser welding due to the complex behaviors which include liquid phase, solid phase and, gas phase. It is necessary to conduct a numerical simulation to understand the detailed procedures of welding. The research was presented the effects of the various potential force models on laser–arc hybrid welding [44] (Figs. 21 and 22).

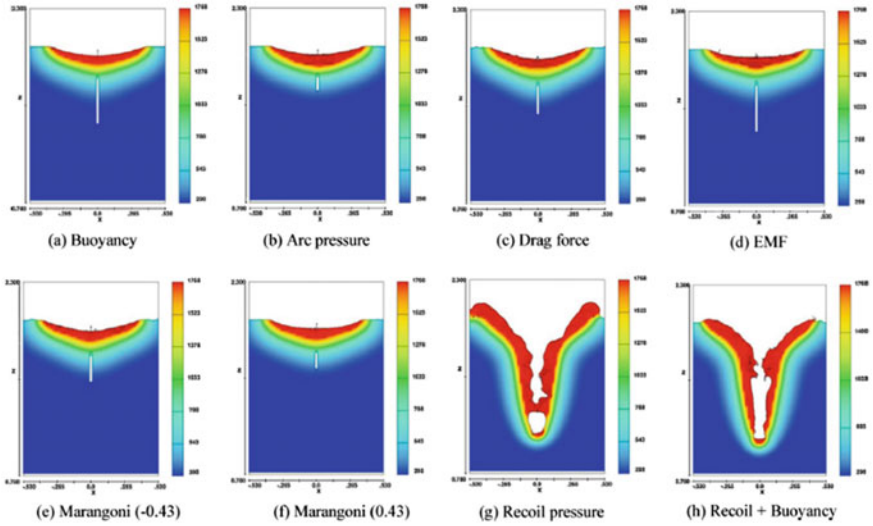

Fig. 21 Effects of potential force models on laser-arc hybrid welding 1

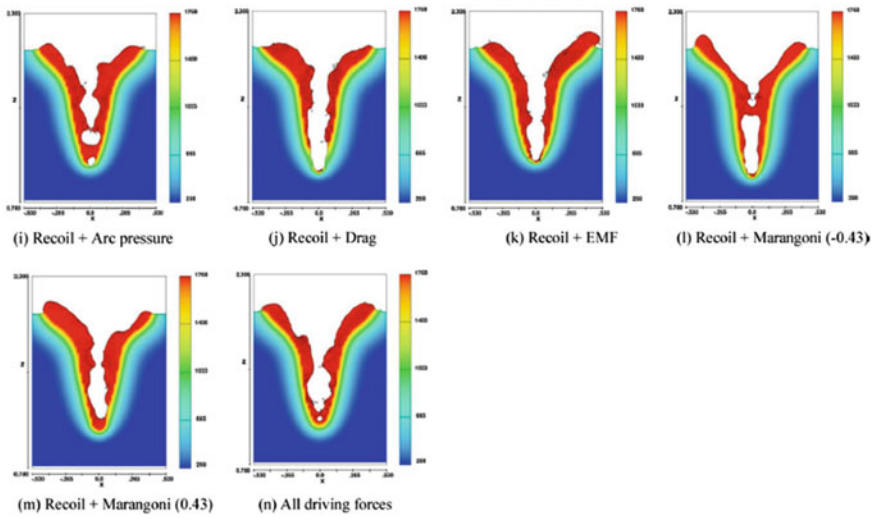

Fig. 22 Effects of potential force models on laser-arc hybrid welding 2

7 Conclusion

A new method of numerical T-M-Me analysis was introduced in this paper. The thermal-metallurgical analysis method was employed in the T-M-Me analysis using real-time temperature and phase fraction history based on the CFD-FEM framework. The suggested core elements of analysis model are summarized below.

- Measurement based process models' parameter
- CFD based mass and heat transfer analysis
- CFD-FEM framework
- Binary search algorithm based data transfer scheme
- Heating rate dependent austenization critical temperature
- New concept of thermal-metallurgical strain behavior

Also, the recent CFD-based process analyses and results that can be extended to multi-physical analysis were briefly introduced. By using the combination of suggested T-M-Me analysis method and CFD welding analysis, it is possible to reproduce a phenomenon closer to reality. However, considerable assumptions and simplified models have differences from real welding phenomena. To solve this gap and to use welding simulation as a prediction tool rather than a reproduction, many young researchers will need to challenge.

Acknowledgements The authors gratefully acknowledge the support of the Brain Korea 21 plus program and Mid-career Researcher Program through NRF of Korea (2013R1A2A1A01015605).

References

1. Rohde J, Jeppsson A (2000) Literature review of heat treatment simulations with respect to phase transformation, residual stresses and distortion. Scand J Metall 29(2):47–62
2. Cho SH, Kim JW (2002) Analysis of residual stress in carbon steel weldment incorporating phase transformations. Sci Technol Weld Joining 7(4):212–216
3. Deng D (2009) FEM prediction of welding residual stress and distortion in carbon steel considering phase transformation effects. Mater Des 30(2):359–366
4. Taljat B, Radhakrishnan B, Zacharia T (1998) Numerical analysis of GTA welding process with emphasis on post-solidification phase transformation effects on residual stresses. Mater Sci Eng A 246(1):45–54
5. Yaghi A, Hyde T, Becker A et al (2008) Finite element simulation of welding and residual stresses in a P91 steel pipe incorporating solid-state phase transformation and post-weld heat treatment. J Strain Anal Eng Des 43(5):275–293
6. Tsirkas SA, Papanikos P, Kermanidis T (2003) Numerical simulation of the laser welding process in butt-joint specimens. J Mater Process Technol 134:59–69
7. Goldak J, Chakravarti A, Bibby M (1984) A new finite element model for welding heat sources. Metall Trans B 15(2):299–305
8. Cho YT, Na SJ (2005) Application of Abel inversion in real-time calculations for circularly and elliptically symmetric radiation sources. Meas Sci Technol 16(3):878–884
9. Cho DW, Lee SH, Na SJ (2013) Characterization of welding arc and weld pool formation in vacuum gas hollow tungsten arc welding. J Mater Process Technol 213(2):143–152

10. Deng D, Murakawa H (2006) Prediction of welding residual stress in multi-pass butt-welded modified 9Cr–1Mo steel pipe considering phase transformation effects. Comput Mater Sci 37 (3):209–219
11. Miyao K, Wang Z, Inoue T (1986) Analysis of temperature, stress and metallic structure in carburized-quenched gear considering transformation plasticity. J Soc Mat Sci Jpn 35 (399):1352–1357
12. Nagasaka Y, Brimacombe J, Hawbolt E et al (1993) Mathematical model of phase transformations and elastoplastic stress in the water spray quenching of steel bars. Metall Trans A 24(4):795–808
13. Kang SH, Im YT (2007) Three-dimensional thermo-elastic–plastic finite element modeling of quenching process of plain-carbon steel in couple with phase transformation. Int J Mech Sci 49(4):423–439
14. Yang QX, Yao M, Park JK (2004) Numerical simulations and measurements of temperature and stress field in medium-high carbon steel specimen after hard-face-welding. Comput Mater Sci 29(1):37–42
15. Deng D, Murakawa H (2008) Finite element analysis of temperature field, microstructure and residual stress in multi-pass butt-welded 2.25 Cr–1Mo steel pipes. Comput Mater Sci 43 (4):681–695
16. Deng D, Murakawa H (2013) Influence of transformation induced plasticity on simulated results of welding residual stress in low temperature transformation steel. Comput Mater Sci 78:55–62
17. Fischer F, Oberaigner E, Tanaka K et al (1998) Transformation induced plasticity revised an updated formulation. Int J Solids Struct 35(18):2209–2227
18. Fischer F, Reisner G, Werner E et al (2000) A new view on transformation induced plasticity (TRIP). Int J Plast 16(7):723–748
19. Cheon J, Kiran DV, Na SJ (2016) Thermal metallurgical analysis of GMA welded AH36 steel using CFD–FEM framework. Mater Des 91:230–241
20. Cheon J, Na SJ (2016) Influence of simulation methods of temperature distribution on thermal and metallurgical characteristics in GMA welding. Mater Des 108:183–194
21. Cheon J, Na SJ (2017) Prediction of welding residual stress with real-time phase transformation by CFD thermal analysis. Int J Mech Sci 131(132):37–51
22. Standard ASTM E407 (2007) Standard practice for microetching metals and alloys. ASTM International. https://doi.org/10.1520/E0407-07
23. Hirt C, Nichols B (1988) Flow-3D user's manual. Flow Science Inc
24. Cho MH, Lim YC, Farson DF (2006) Simulation of weld pool dynamics in the stationary pulsed gas metal arc welding process and final weld shape. Weld J 85(12):271–283
25. Kikuchi N (1986) Finite element methods in mechanics. CUP Archive
26. Patankar S (1980) Numerical heat transfer and fluid flow. CRC Press
27. Cormen TH, Leiserson CE, Rivest RL et al (2001) Introduction to algorithms. MIT Press, Cambridge
28. Oliveira FLG, Andrade MS, Cota AB (2007) Kinetics of austenite formation during continuous heating in a low carbon steel. Mater Charact 58(3):256–261
29. Macedo MQ, Cota AB, Araújo FGDS (2011) The kinetics of austenite formation at high heating rates. Rem—Revista Escola de Minas 64(2):163–167
30. Cho DW, Na SJ, Cho MH et al (2013) Simulations of weld pool dynamics in V-groove GTA and GMA welding. Weld World 57(2):223–233
31. Cho DW, Na SJ (2015) Molten pool behaviors for second pass V-groove GMAW. Int J Heat Mass Transf 88:945–956
32. Wu L, Cheon J, Kiran DV et al (2016) CFD simulations of GMA welding of horizontal fillet joints based on coordinate rotation of arc models. J Mater Process Technol 231:221–238
33. Cho DW, Song WH, Cho MH et al (2013) Analysis of submerged arc welding process by three-dimensional computational fluid dynamics simulations. J Mater Process Technol 213 (12):2278–2291

34. Kiran DV, Cho DW, Song WH et al (2014) Arc behavior in two wire tandem submerged arc welding. J Mater Process Technol 214(8):1546–1556
35. Kiran DV, Cho DW, Song WH et al (2015) Arc interaction and molten pool behavior in the three wire submerged arc welding process. Int J Heat Mass Transf 87:327–340
36. Cho DW, Kiran DV, Na SJ (2017) Analysis of molten pool behavior by flux-wall guided metal transfer in low-current submerged arc welding process. Int J Heat Mass Transf 110:104–112
37. Cho DW, Na SJ, Cho MH et al (2013) A study on V-groove GMAW for various welding positions. J Mater Process Technol 213(9):1640–1652
38. Cheon J, Kiran DV, Na SJ (2016) CFD based visualization of the finger shaped evolution in the gas metal arc welding process. Int J Heat Mass Transf 97:1–14
39. Ahn JS, Na SJ (2013) Three-dimensional thermal simulation of nanosecond laser ablation for semitransparent material. Appl Surf Sci 283:115–127
40. Han SW, Ahn JS, Na SJ (2016) A study on ray tracing method for CFD simulations of laser keyhole welding: progressive search method. Weld World 60(2):247–258
41. Han SW, Cho WI, Na SJ et al (2013) Influence of driving forces on weld pool dynamics in GTA and laser welding. Weld World 57(2):257–264
42. Zhang YX, Han SW, Cheon J et al (2017) Effect of joint gap on bead formation in laser butt welding of stainless steel. J Mater Process Technol 249:274–284
43. Ge W, Han SW, Fang Y et al (2017) Mechanism of surface morphology in electron beam melting of Ti6Al4 V based on computational flow patterns. Appl Surf Sci 419:150–158
44. Cho DW, Cho WI, Na SJ (2014) Modeling and simulation of arc: laser and hybrid welding process. J Manufact Process 16(1):26–55